Accurate simulation of Resonance-Raman spectra of flexible molecules: an internal coordinates approach

Alberto Baiardi,*,† Julien Bloino,‡,† and Vincenzo Barone†

†*Scuola Normale Superiore, Piazza dei Cavalieri 7, I-56126 Pisa, Italy*

‡*Consiglio Nazionale delle Ricerche, Istituto di Chimica dei Composti OrganoMetallici (ICCOM-CNR), UOS di Pisa, Area della Ricerca CNR, Via G. Moruzzi 1, I-56124 Pisa, Italy*

E-mail: alberto.baiardi@sns.it

Abstract

The interpretation and analysis of experimental resonance Raman (RR) spectra can be significantly facilitated by vibronic computations based on reliable quantum mechanical (QM) methods. With the aim of improving the description of large and flexible molecules, our recent time-dependent formulation to compute vibrationally resolved electronic spectra, based on cartesian coordinates, has been extended to support internal coordinates. A set of non-redundant delocalized coordinates is automatically generated from the molecular connectivity thanks to a new general and robust procedure. In order to validate our implementation, a series of molecules has been used as test cases. Among them, rigid systems show that normal modes based on cartesian and delocalized internal coordinates provide equivalent results, but the latter set is much more convenient and reliable for systems characterized by strong geometric deformations associated to the electronic transition. The so-called Z-matrix internal

coordinates, which perform well for chain molecules, are also shown to be poorly suited in presence of cycles or non-standard structures.

1 Introduction

Raman spectroscopy and its resonant (RR) counterpart, in which the incident light matches an electronic transition to a so-called intermediate state, are increasingly used for the analysis of complex systems of biological[1–5] and/or technological interests,[6] not to mention cultural heritage,[7,8] where it is nearly systematically employed. In particular, RR shows enhancements of the scattered intensity by factors of 10^3 to 10^6 with respect to the conventional non-resonant Raman spectroscopy (also referred to as nRR in the following), and only the intensities of the vibrational modes associated to intense vibronic transitions between the initial and intermediate electronic states are actually observed.[9,10] As a consequence, it is possible to analyze specific regions of the whole molecular system by tuning the incident radiation to match the corresponding electronic transitions localized on the target moiety.[11,12] The initial and final states of a RR transition are different vibrational levels of the same electronic ground state, but the spectrum will change depending on the intermediate electronic state.[13] As a consequence, a RR spectrum conveys information about both ground and excited electronic states with a resolution much higher than that of the corresponding one-photon absorption (OPA) spectrum. The main drawback of RR with respect to nRR or infrared (IR) spectroscopies is the lack of simple selection rules[14] with the consequence of being more difficult to interpret. In this connection, quantum-mechanical (QM) simulations can play an invaluable role, provided that they are able to take into account all the effects (stereo-electronic, vibronic, environmental), which contribute to the overall spectrum.[13,15] Methods rooted into the density functional theory (DFT) and its time-dependent extension (TD-DFT) are robust enough to provide reliable electronic structure results.[16–18] Besides, their coupling with molecular mechanics (MM) force fields[19,20] and polarizable continuum models (PCM)[21,22] to embed the active region (e.g. the chromophore) to get a reliable description of the environment are paving the way to the treatment of larger and larger systems both in the gas phase and in solution.[23–25]

Regarding the actual computation of vibronic spectra, both time-independent (TI)[26–28]

and time-dependent (TD)[29–31] routes have been proposed. In order to provide a comprehensive and easy-to-use tool to carry out such calculations, a platform has been built in our group, supporting both routes and including all the terms playing a significant role at the harmonic level, namely the Franck-Condon and Herzberg-Teller effects, including normal modes mixing, also known as Duschinsky mixing, between the electronic states involved in the transitions,[32–35] as well as the leading anharmonic contributions.[36–38] The two approaches (TI and TD) are often complementary in most spectroscopies, such as OPA, with the former providing details for the band assignment and allowing the simulation of high-resolution band-shapes (narrow bands), while the latter offers a straightforward inclusion of temperature effects and does not suffer from the problem of truncation of infinite summations.[18] For the spectroscopy of interest here, that is RR, both TI and TD routes provide the same set of information so that the choice of one over the other depends on its numerical stability. In this regard, the time-dependent formulation can be preferred due to the difficulty of assessing the reliability of the prescreening used to choose the most relevant transitions in the infinite summations present in the time-independent case.

The most reliable and robust vibronic models developed until now for large systems have been based on cartesian normal modes, easier to handle in black-box implementations for any kind of semi-rigid system. However, internal coordinates are much more effective for flexible systems or in presence of large deformations between the ground and excited electronic states. Even if some pilot studies have been performed for OPA spectra employing internal coordinates with promising results,[39–41] to the best of our knowledge, RR spectra have not yet been investigated in this connection. Moreover, black-box procedures generating non-redundant internal coordinates have not yet been applied to vibronic computations. However, in our opinion this is a mandatory condition for the systematic use of this approach on large systems. Starting from current approaches for geometry optimizations employing redundant internal coordinates built automatically from the molecular connectivity,[42–44] we have devised a general procedure to define a set of non-redundant coordinates. On these

grounds, we report here the first RR spectra obtained from this new procedure employing delocalized internal coordinates and including all the harmonic contributions in a general TD framework. Inclusion of solvent effects by means of PCM is also considered.

The paper is organized as follows. The theoretical background is summarized in section 2, with special reference to the definition of the harmonic TD model in internal coordinates, and to the selection of a non-redundant subset of the latter. The computational details are presented in section 3. Three test cases (5,6-dimethyluracil, imidazole and tris(bipyrimidine)ruthenium(II) chloride) are discussed in section 4, while conclusions and perspectives are collected in section 5.

2 Theory

2.1 Simulation of the RR spectra

The experimental quantity, which is usually reported from a Raman experiment is the differential cross section σ, which is proportional to the scattered intensity $I_s(\omega_I, \omega_s)$, which in turns depends on the incident and scattered frequencies, ω_I and ω_s, respectively. I_s is related to the transition polarizability tensor $\boldsymbol{\alpha}^{if}$ through the following expression:

$$I_s\left(\frac{\pi}{2}; \|^s + \perp^s; \perp^I \omega_I; \omega_s\right) = k{\omega_s}^2 I_{\text{inc}} \frac{45a^2 + 7g^2 + 5d^2}{45} \tag{1}$$

where, for the sake of simplicity, we have assumed that the polarization of the incident light is perpendicular to the direction of scattering, and that the scattered light is unpolarized. The three invariants a (mean isotropic polarizability), g (symmetric anisotropy) and d (symmetric anisotropy) are related to the elements of the transition polarizability tensor through the following expression:[9]

$$
\begin{aligned}
a &= \frac{1}{3}\left(\alpha_{xx}^{if} + \alpha_{yy}^{if} + \alpha_{zz}^{if}\right) \\
g^2 &= \frac{1}{2}\left(\left|\alpha_{xx}^{if} - \alpha_{yy}^{if}\right|^2 + \left|\alpha_{xx}^{if} - \alpha_{zz}^{if}\right|^2 + \left|\alpha_{zz}^{if} - \alpha_{yy}^{if}\right|^2\right) \\
&\quad + \frac{3}{4}\left(\left|\alpha_{xy}^{if} + \alpha_{yx}^{if}\right|^2 + \left|\alpha_{xz}^{if} + \alpha_{zx}^{if}\right|^2 + \left|\alpha_{yz}^{if} + \alpha_{zy}^{if}\right|^2\right) \\
d^2 &= \frac{3}{4}\left(\left|\alpha_{xy}^{if} - \alpha_{yx}^{if}\right|^2 + \left|\alpha_{xz}^{if} - \alpha_{zx}^{if}\right|^2 + \left|\alpha_{yz}^{if} - \alpha_{zy}^{if}\right|^2\right)
\end{aligned}
\tag{2}
$$

Different routes to calculate $\boldsymbol{\alpha}^{if}$ have been proposed. Among them, let us recall the so-called time-independent (TI) methods, in which the polarizability tensor is calculated as a sum over all the vibrational levels of the intermediate electronic state, reported below:

$$
\alpha_{\rho\sigma}^{if} = \frac{1}{\hbar}\sum_{n(\underline{m})} \frac{\langle\, \psi_{f(\underline{0})} \mid \mu^e_{\underline{m}\,\underline{0},\rho} \mid \psi_{n(\underline{m})} \,\rangle \langle\, \psi_{n(\underline{m})} \mid \mu^e_{\underline{m}\,\underline{0},\sigma} \mid \psi_{i(\underline{0})} \,\rangle}{\omega_{ni} - \omega_I - i\gamma} \tag{3}
$$

where the initial and intermediate electronic states are labelled as $\underline{0}$ and $\underline{m}$, γ is the lifetime of the latter (and assumed independent of the vibrational state), and $\boldsymbol{\mu}^e_{\underline{m}\,\underline{0}}$ is the transition electric dipole moment between them. Finally, $\mid \psi_{i(\underline{0})} \,\rangle$ and $\mid \psi_{f(\underline{0})} \,\rangle$ are the vibrational levels involved in the Raman transition, whereas $\mid \psi_{n(\underline{m})} \,\rangle$ are vibrational levels of the intermediate state.

The infinite summation involved in equation 3 requires a selection of the intermediate levels, giving the main contributions to $\boldsymbol{\alpha}^{if}$. Conversely, a time-dependent (TD) formulation can be derived starting from equation 3.[9] The tensor $\boldsymbol{\alpha}^{if}$ can be expressed as the half-Fourier transform of the time-dependent transition dipole moment cross-correlation function, that is:

$$
\alpha_{\rho\sigma}^{if} = \frac{i}{\hbar^2}\int_0^{+\infty} \mathrm{d}t \,\langle\, \psi_{f(\underline{0})} \mid \mu^e_{\underline{m}\,\underline{0},\rho} e^{-i\hat{H}_m t/\hbar} \mu^e_{\underline{m}\,\underline{0},\sigma} \mid \psi_{i(\underline{0})} \,\rangle\, e^{-it(\omega_{\mathrm{ad}} - \omega_I - i\gamma)} \tag{4}
$$

where ω_{ad} is the adiabatic energy separation between the electronic states and $e^{-i\hat{H}_m t/\hbar}$ is the time evolution operator on the intermediate state PES. As shown in the pioneering

work of Heller and co-workers,[45] the cross-correlation function can be computed analitically at different levels of approximations. Even if semi-classical theories have been used to simulate the time-evolution of the cross-correlation function,[46–48] also full-quantum expressions have been derived by Heller,[49] by neglecting temperature effects and using the harmonic approximation. Even if those accurate formulations have been available for thirty years, the application of the TD theory to the simulation of RR spectra has been usually limited to approximated models, neglecting either frequency changes between the two electronic states[50] or mode-mixing effects.[30,51] Only recently, the inclusion of those effects, as well as the extension to Herzberg-Teller contributions, have been discussed.[31,52,53] Similarly, we have extended our general time-dependent framework, previously derived for the calculation of one-photon spectra[35] and based on the Feynmann path integral theory, to the calculation of RR spectra.[54] Thanks to its generality, both mode-mixing and Herzberg-Teller effects could be straightforwardly included within this framework.

2.2 Harmonic models in internal coordinates

In order to make the discussion below easier to follow, it is necessary to introduce at this point some general aspects concerning the description of the vibronic transition. Indeed, the PESs of the initial and intermediate states are different as the molecule undergoes changes upon the electronic transition and their respective minima may not be superimposed. Due to the limitations of the harmonic approximation of the PES, one needs to choose between two representations. In the adiabatic models, the PES of the intermediate state is expanded about its own equilibrium position (Adiabatic Hessian, AH), while in the vertical ones it is expanded about the equilibrium geometry of the initial state (Vertical Hessian, VH). In both cases, simplified models, where mode-mixing effects are neglected, can be derived (Adiabatic Shift, AS and Vertical Gradient, VG, respectively).[33,34] In the following, we will mostly consider adiabatic models to describe the vibronic transition.

Within the vibronic models presented above, the molecular vibrations are expressed in

terms of cartesian normal modes. However, as noted by various authors,[39,40,55] cartesian coordinates are often ill-suited for the study of large, flexible molecules since large-amplitude normal-modes are poorly described in terms of linear combinations of cartesian coordinates. A remarkable improvement is obtained by using an appropriate set of internal coordinates. However, in order to support a more general, non-orthogonal coordinate set, the available theoretical framework must be generalized. In fact, when normal modes are expressed in terms of a curvilinear set of internal coordinates, the matrix $\mathbf{J}$ defining the rotation of normal modes from the initial to the final (or intermediate) electronic state can be significantly different, with the possibility of not being orthogonal anymore. An effective definition of the so-called Duschinsky transformation in terms of non-orthogonal coordinates has been proposed by Reimers,[56] based on the well-known Wilson theory of internal coordinates.[14] First of all, the non-orthogonal internal coordinates $\mathbf{s}$ are expanded as Taylor series in power of the cartesian ones $\mathbf{x}$:

$$s_i = \sum_{j=1}^{3N_a} \left(\frac{\partial s_i}{\partial x_j}\right)_{\text{eq}} (x_j - x_{j,\text{eq}}) + \frac{1}{2} \sum_{j,k=1}^{3N_a} \left(\frac{\partial^2 s_i}{\partial x_j \partial x_k}\right)_{\text{eq}} (x_j - x_{j,\text{eq}})(x_k - x_{k,\text{eq}}) + \bigcirc\left(\mathbf{x}^3\right) \quad (5)$$

The Jacobian of the transformation between the coordinate set $\mathbf{x}$ and $\mathbf{s}$ is usually called the Wilson matrix $\mathbf{B}$, whose elements are $B_{ij} = \left(\partial s_i/\partial x_j\right)_{\text{eq}}$, whereas the tensor containing the second-order terms $\left(\partial^2 s_i/\partial x_j \partial x_k\right)_{\text{eq}}$ is usually referred to as $\mathbf{B}'$. In the following, we will call linearized internal coordinates the first-order approximation of the internal coordinates in terms of the cartesian ones. The $\mathbf{B}$ matrix is sufficient to transform the gradient ($\mathbf{g}$) between cartesian and internal coordinates. However, both $\mathbf{B}$ and $\mathbf{B}'$ are required to obtain the Hessian matrix in internal coordinates $\mathbf{H_s}$ starting from the Hessian in cartesian coordinates $\mathbf{H_x}$,[57,58] except for stationary points of the PES, where only $\mathbf{B}$ needs to be computed,[41] and the transformation is given by the following relation:

$$\mathbf{H_s} = \mathbf{B}^T \mathbf{H_x} \mathbf{B} \tag{6}$$

Since in the following we will focus on adiabatic models, equation 6 can be safely used. Let us introduce also the Wilson matrix $\mathbf{G}$, defined as $\mathbf{G} = \mathbf{B}\mathbf{M}^{-1}\mathbf{B}^T$, which is the zeroth-order approximation of the metric matrix of the curvilinear coordinate set, and $\mathbf{M}$ is the diagonal matrix of the atomic masses. Finally, the internal coordinate normal modes $\mathbf{L_s}$ are the eigenvectors of the $\mathbf{GH_s}$ matrix.[14,59] Since $\mathbf{GH_s}$ is, in general, non-symmetric, $\mathbf{L_s}$ is not orthogonal.

The Duschinsky matrix and the shift vector in internal coordinates, $\mathbf{J_s}$ and $\mathbf{K_s}$ respectively, can be calculated following the same strategy as in the cartesian case, with their final expressions given as,

$$\mathbf{J_s} = \bar{\mathbf{L}}_\mathbf{s}^{-1} \bar{\bar{\mathbf{L}}}_\mathbf{s} \qquad\qquad \mathbf{K_s} = \bar{\mathbf{L}}_\mathbf{s}^{-1} \left(\bar{\bar{\mathbf{s}}}_{\mathrm{eq}} - \bar{\mathbf{s}}_{\mathrm{eq}} \right) \tag{7}$$

where quantities relative to the initial state (also the final one) are labelled with a single overbar, and the ones relative to the intermediate state with a double overbar. Note that here, masses are not present in the definition of the shift vector $\mathbf{K_s}$. Furthermore, this expression for the Duschinsky matrix holds only for adiabatic models. As already pointed out,[41] for adiabatic models, it is possible to express $\mathbf{L_s}$ in terms of $\mathbf{L_x}$, the transformation matrix between the mass-weighted normal coordinates and cartesian coordinates, as follows:

$$\mathbf{L_s} = \mathbf{B}\mathbf{M}^{-1/2}\mathbf{L_x} \tag{8}$$

Starting from equation 8 and using the relation given in equation 7, $\mathbf{J_s}$ can be easily expressed in terms of the cartesian normal modes as follows:

$$\mathbf{J_s} = \bar{\mathbf{L}}_\mathbf{x}^T \mathbf{M}^{1/2} \bar{\mathbf{B}}^{-1} \bar{\bar{\mathbf{B}}} \mathbf{M}^{-1/2} \bar{\bar{\mathbf{L}}}_\mathbf{x} \tag{9}$$

As a consequence, $\mathbf{J_x} = \mathbf{J_s}$ only when $\overline{\mathbf{B}}^{-1}\overline{\overline{\mathbf{B}}} = \mathbf{I}$. The previous equality does not hold in the general case, since internal coordinates are curvilinear, and therefore the $\mathbf{B}$ matrix changes with the reference geometry. Let us remark that the difference between $\mathbf{B}$ matrices calculated at two different geometries is negligible only for slight distortions from the equilibrium position, and only in this case is the Duschinsky matrix equal in both internal and cartesian coordinates. However, when large-amplitude distorsions are present, $\mathbf{J_x}$ and $\mathbf{J_s}$ can be significantly different.

Let us consider now the definition of $\mathbf{K_s}$ given in equation 7, which holds for both adiabatic and vertical models. In the adiabatic case, the equilibrium geometry of the intermediate state $\bar{\bar{\mathbf{s}}}_{\mathrm{eq}}$ is calculated explicitly and equation 8 can be used to express the shift vector as,

$$\mathbf{K_s} = \overline{\mathbf{L}}_{\mathbf{x}}^{T}\mathbf{M}^{1/2}\overline{\mathbf{B}}^{-1}\left(\bar{\bar{\mathbf{s}}}_{\mathrm{eq}} - \bar{\mathbf{s}}_{\mathrm{eq}}\right) \tag{10}$$

Hence, $\mathbf{K_x} = \mathbf{K_s}$ only when $\bar{\bar{\mathbf{s}}}_{\mathrm{eq}} - \bar{\mathbf{s}}_{\mathrm{eq}} = \overline{\mathbf{B}}\left(\bar{\bar{\mathbf{x}}}_{\mathrm{eq}} - \bar{\mathbf{x}}_{\mathrm{eq}}\right)$. This is not the case for adiabatic models, since the curvilinear internal coordinates corresponding to the equilibrium geometries of the two electronic states are calculated explicitly, and are in general different from their linearized approximations.

Regarding vertical models, we will limit our discussion to the Vertical Gradient approximation here. In this setting, the Hessian of the intermediate state is assumed to be the same as the initial state's ($\mathbf{J} = \mathbf{I}$), and the equilibrium geometry $\bar{\bar{\mathbf{s}}}_{\mathrm{eq}}$ is extrapolated using the intermediate state gradient. Following the same procedure as in the cartesian case,[34] and using the internal coordinates gradient $\bar{\bar{\mathbf{g}}}_{\mathbf{s}}$ instead of the cartesian one $\bar{\bar{\mathbf{g}}}_{\mathbf{x}}$, $\mathbf{K_s}$ is given by:

$$\mathbf{K_s} = -\overline{\overline{\mathbf{\Omega}}}^{-2}\bar{\bar{\mathbf{g}}}_{\mathbf{q}} = -\overline{\overline{\mathbf{\Omega}}}^{-2}\overline{\mathbf{L}}_{\mathbf{s}}^{T}\bar{\bar{\mathbf{g}}}_{\mathbf{s}} \tag{11}$$

where $\bar{\bar{\mathbf{g}}}_{\mathbf{q}}$ is the gradient of the intermediate state expressed in terms of the final state's curvilinear normal coordinates and $\overline{\overline{\mathbf{\Omega}}}$ is the diagonal matrix containing the frequencies along

the diagonal. By using equation 8 to write $\mathbf{L_s}$ in terms of $\mathbf{L_x}$, and employing the well-known relation between the gradient in internal and cartesian coordinates $\mathbf{g_x} = \mathbf{B}^T\mathbf{g_s}$,[60] it is possible to prove that, at the VG level, the definition of the shift vector is the same in cartesian and internal coordinates. As a consequence, in the following, the coordinate set used in VG calculations will not be specified. This strict equivalence has been overlooked in previous studies[40,41,61,62] and explains the claimed accuracy of the VG implementation in cartesian coordinates.

2.3 Selection of non-redundant internal coordinates

The relations given in equation 7 hold if the internal coordinate set is non-redundant, and therefore $\mathbf{B}$ is a square, invertible matrix. However, while the definition of cartesian coordinates is univocal, internal coordinates are usually redundant, since their number is larger than the vibrational degrees of freedom of the molecule. As a consequence, a non-redundant subset must be defined before performing any vibronic calculation. Let us remark that this step is not univocal, and different non-redundant sets of internal coordinates can be defined starting from the same initial redundant set.

In the following, we will use as redundant set of coordinates the so-called primitive internal coordinates (PICs), which includes all bond lengths, valence angles and dihedral angles, and are defined univocally once the molecular topology is built. Furthermore, for each tri-coordinated center, a symmetric out-of-plane coordinate is added.

Once the PICs are built, a procedure to extract a non-redundant subset of coordinates must be provided, for instance, by using the schemes adopted by geometry optimization algorithms.[42,63,64] However, even if some of these approaches have been applied to computational spectroscopy,[65–69] the systematic analysis of their reliability in the field of vibronic spectroscopy has been scarce.

In this work, we will use two different non-redundant sets of internal coordinates. The first one is built from the so-called Z-matrix internal coordinates (ZIC),[70] and includes all

the variables defined in a Z-matrix. This set is non-redundant since, for non-linear molecules, a standard Z-matrix provides $N_{\rm at}-1$ stretchings, $N_{\rm at}-2$ bendings and $N_{\rm at}-3$ torsions. As a consequence, the total number of internal coordinates is equal to the number of vibrational degrees of freedom ($N_{\rm vib}$). ZICs have been widely used in geometry optimization algorithms, but some limitations make their general use difficult.[71] First of all, it is not straightforward to build a complete, non-redundant Z-matrix in an automatic way, especially for large systems, which make ZICs ill-suited for black-box, automatized implementations. Next, when dealing with molecules characterized by a complex topology (like cycles or condensed rings), the efficiency of optimization algorithms using Z-matrix coordinates is usually poor and can only be improved by building *ad-hoc* Z-matrices, for instance with the help of dummy atoms.[70,71]

The second set of non-redundant internal coordinates which will be used here is built from the so-called delocalized internal coordinates (DICs),[42,43] whose definition is based on the singular value decomposition (SVD) algorithm to identify the redundancies. In order to understand how it works, let us consider the matrix $\mathbf{B}\mathbf{B}^T$ that we want to diagonalize:

$$\left(\mathbf{B}\mathbf{B}^T\right)\mathbf{v} = \mathbf{v}\mathbf{\Lambda} \tag{12}$$

The columns of $\mathbf{v}$ are the eigenvectors $\mathbf{v}_i$ and $\mathbf{\Lambda}$ is the diagonal matrix of the eigenvalues. It can be proven that the number of non-zero eigenvalues of $\mathbf{\Lambda}$ is equal to the number of independent degrees of freedom of the PICs, and is therefore equal to $N_{\rm vib}$ if the PICs are correctly defined. Furthermore, the eigenvectors corresponding to non-zero eigenvalues define a non-redundant set of internal coordinates $\mathbf{s}'$, which can be expressed as linear combinations of the $\mathbf{s}$ coordinates,

$$\mathbf{s}' = \mathbf{v}'^T\mathbf{s} \tag{13}$$

where $\mathbf{v}'$ is a $n_{\rm PIC}\times N_{\rm vib}$ matrix, whose columns are the eigenvectors of $\mathbf{B}\mathbf{B}^T$ corresponding to non-zero eigenvalues. This set of internal coordinates is usually referred to as delocalized

since it includes in general coordinates where PICs of different type and localized on different sites of the molecule are mixed. In this connection, it is noteworthy that the property outlined above still holds even by using $\mathbf{BuB}^T$ instead of $\mathbf{BB}^T$, where $\mathbf{u}$ is a general, non-singular $n_{\mathrm{PIC}} \times n_{\mathrm{PIC}}$ matrix and, by changing $\mathbf{u}$, different sets of internal coordinates are obtained.[64,72] However, in this work only the standard DICs will be used.

In conclusion, it should be remarked that, in order to generate DICs, the equilibrium geometry of one of the two electronic states is taken as a reference to build the Wilson matrix $\mathbf{B}$ and the resulting internal coordinate set is then used to describe both electronic states. This issue is not present in the simulation of other vibrational spectroscopies (like infrared, vibrational circular dichroism or non-resonant Raman) or in geometry optimizations, since in those cases only one reference geometry is present.

3 Computational details

All electronic structure and vibronic spectra calculations were performed with the development version of the GAUSSIAN suite of quantum chemical programs.[73] The density functional theory (DFT), for the ground states, and its time-dependent extension (TD-DFT), for the excited states, were used for the electronic calculations, using the B3LYP exchange-correlation functional.[74] The SNSD basis set,[75] developed in our group to study spectroscopic properties of medium- and large-size molecular systems, has been used. This basis set has been built from the polarized double-ζ basis set N07D,[76,77] with the inclusion of diffuse s functions on all atoms, and one set of diffuse polarization functions (d on heavy atoms and p on hydrogens) and aims at providing a good balance between accuracy and computational cost. For the sake of coherence with our previous works,[78] the aug-cc-pVTZ basis set[79] has been used for all calculations on imidazole.

Solvation effects have been included in the QM calculations by means of the polarizable continuum model (PCM).[22,80] In particular, its integral-equation formulation (IEF-PCM)

has been used[81] and the solute cavity has been built by using a set of interlocking spheres centered on the atoms with the following radii (in Å): 1.443 for hydrogen, 1.926 for carbon, 1.750 for oxygen and 1.830 for nitrogen, each scaled by a factor of 1.1, which is the default value inside GAUSSIAN. The value of the solvent static and dynamic dielectric constants used for water in all the calculations are $\epsilon = 78.36$ and $\epsilon_\infty = 1.78$ and the equilibrium solvation regime was adopted. A more detailed discussion regarding the choice of the equilibrium regime in the simulation of RR spectra can be found in ref.[54,78]

Let us remark that, for all TD-RR calculations, only the intensities of the fundamental bands have been computed. Furthermore, following the computational procedure presented in our previous work,[54] a Gauss-Legendre quadrature has been implemented in order to speed-up the calculation of the half-Fourier integral, by reducing the number of sampling points. In all cases, a grid of 2^{12} points with a time spacing of $2.44 \cdot 10^{-16}$ s gave a complete convergence of the integral. Finally, a damping constant of 100 cm^{-1} has been used in all simulations, in agreement with previous works.[82] With higher values for γ, the intensity of each peak is scaled by a constant factor, but the overall band-shape does not change significantly. Thanks to a very effective and parallelized implementation, the actual calculation of the vibronic spectra is done in a negligible time with respect to the generation of the required QM data.[78,83]

As outlined in the previous section, in order to define the non-redundant set of internal coordinates, the molecular topology must be built. For each case considered in the following, two atoms X and Y are defined as bonded if their distance is shorter than 130 % of their average XY bond length. Following the GAUSSIAN default parameters, those averages are taken from B3LYP/6-31G(d) results. In order to calculate the Wilson matrix $\mathbf{B}$ for the non-redundant set of internal coordinates, the well-known analytical expressions for the elements of $\mathbf{B}$ for bond lengths, valence, out-of-plane and dihedral angles (given for example in ref.[14,84]) have been used for both delocalized and Z-matrix internal coordinates. A significant speed-up of the overall computational procedure is achieved by replacing the diagonalization of

$\mathbf{BB}^T$ by its singular value decomposition (SVD). In all cases, a threshold of 10^{-5} on the absolute value of the eigenvalues has been used to select the eigenvectors corresponding to non-zero eigenvalues. Finally, in every simulation, the equilibrium geometry of the electronic ground state has been used to build the Wilson matrix $\mathbf{B}$ used to generate DICs.

Let us remark that, when calculated RR spectra are compared to the corresponding experimental results, the laser wavelength used in the experiment cannot be chosen in the simulations, since the experimental vertical excitation energy is different from the theoretical one. Since it is generally assumed that the incident energy of the laser matches precisely the vertical transition energy, we assume the same here and use the theoretical vertical transition energy for ω_I.[78,85]

The graphical user interface VMS-draw,[86] recently implemented by some of us, has been used to plot the vibronic spectra and to generate the graphical representation of the Duschinsky matrix and of the shift vector.

4 Examples of applications

4.1 5,6-dimethyluracil

The first example, which has been chosen to test the reliability of the theory described above is 5,6-dimethyluracil (5,6-DMU), with the Z-matrix defined in table 1. The study of the electronic properties of nucleobases is of great interest both from a practical and a theoretical points of view.[87–89] First of all, the interaction of nucleobases and their derivatives with UV-vis light is at the heart of most of the DNA photodamage processes, therefore the study of the photochemical properties of nucleobase can give insights into the mechanism of those processes. RR spectroscopy has been applied in the last years to characterize the short-time dynamics of excited states of a large number of nucleobase derivatives.[90–92] Even if several experimental spectra are therefore available, their interpretation usually relies on approximated models,[93–95] which neglect either non-Condon or mode-mixing effects or both

of them. However, since nucleobases usually undergo significant geometry changes upon electronic excitation, a correct description of vibronic properties of such flexible molecules requires the use of an appropriate coordinate system.

Here, we will focus on the RR spectrum of 5,6-DMU with an incident wavelength set to match the $S_2 \leftarrow S_0$ ($n \rightarrow \pi^*$) electronic transition, since experimental data are available only for the resonant case with this state.[92] The equilibrium geometry of the S_2 state has been calculated following the procedure outlined in the computational details, neglecting solvent effects. As shown in figure 1, even if in both electronic states the ring is planar, one of the methyl residues is rotated by $\approx 60^\circ$ upon the excitation. Figure 2 shows the RR spectrum simulated with different models for the intermediate-state PES. As shown in the upper left panel, the theoretical spectrum calculated at the AH level by using cartesian coordinates is dominated by an intense band in the low-energy region, corresponding to normal modes involving the torsion of the methyl groups. The overall band-shape calculated at the VG level, reported in the upper right panel of figure 2, is significantly different from the AH one in cartesian coordinates, since the low-energy intense peak is not present anymore, while various peaks appear in the region between 800 and 2000 cm^{-1}. Let us recall that, when experimental results are poorly reproduced by using adiabatic models in cartesian coordinates due to the presence of large-amplitude deformations, vertical models in cartesian coordinates are usually employed instead to obtain more reliable results.[41,61] In fact, in vertical models, the normal modes of the two PESs are defined with respect to the same reference geometry, and, as a consequence, the inaccurate description of large-amplitude distorsions in cartesian coordinates is partially recovered. However, in this case, as can be shown by comparison of the upper right and the lower right panels of figure 2, the RR spectrum calculated at the AH level by using delocalized internal coordinates is not equivalent to the VG one. The differences between the two theoretical spectra are mainly due to the strong influence of mode-mixing effects, and therefore the VG model is ill-suited to reproduce the spectrum. On the other hand, use of the more refined Vertical Hessian

model in cartesian coordinates, which includes mode-mixing effects, is not straightforward due to the presence of four imaginary frequencies at the ground-state geometry, which would require the inclusion of anharmonic terms in the expansion of the excited-state PES.

In order to check the accuracy of the results obtained with different coordinate systems and models for the excited-state PES, the theoretical results have been compared to the experimental data, taken from ref.[92] Since the experimental spectrum has been recorded in water, solvent effects have been taken into account by means of PCM, following the protocol described in the computational details. When solvent effects are included, the equilibrium geometry of the excited state is significantly different since the six-term ring undergoes a distortion from the planar geometry upon the electronic excitation, and the rotation of one of the methyl groups is still present. The theoretical results obtained in aqueous solution are reported in figure 3. As shown in the left panel, the agreement between the theoretical results obtained with the AH model in cartesian coordinates and the experimental spectrum is rather poor. Conversely, the agreement becomes significantly better when DICs are used in the AH model, as reported in the right panel. In order to check the influence of the internal coordinate sets, the spectrum obtained with ZICs is reported as well, in the left panel. First of all, the Z-matrix which has been used (see table 1 for its definition) is a standard one, and no dummy atoms are introduced in order to keep the correct symmetry of the system. In fact, our goal is to compare the performance of automatized algorithms for the generation of internal coordinates, and therefore, no *ad-hoc* Z-matrices have been used. The ZIC spectrum reported in the left panel of figure 3 shows that the use of Z-matrix coordinates does not improve the agreement between experimental and theoretical results. In particular, the most intense bands are still observed in the 900-1100 cm^{-1} spectrum range, compared to about 1700 cm^{-1} in the DIC case and in experiment. In fact, as previously pointed out, Z-matrix coordinates are poorly suited for the description of ring deformations, since one of the bond lengths and valence angles involving ring atoms are not included in the definition of the internal coordinates, and therefore DICs are more suitable when electronic

excitations are associated to ring deformations.

In conclusion, it should be noted that slight differences between theoretical and experimental results are still present, even if DICs are used. Indeed, the intensity of the bands under 1200 cm^{-1} is underestimated, and an additional band at about 1480 cm^{-1} is present in the theoretical spectrum. It is possible to further improve the accuracy by refining this model. First of all, the calculations have been performed at the Franck-Condon level, and therefore the Herzberg-Teller contributions have not been investigated. Another limitation lies in the description of solvent effects by means of PCM, since some first-shell water molecules interact specifically with the solute, which are poorly reproduced by continuum models.[21,22] Therefore, the inclusion of at least part of the first solvation shell in the QM part of the calculation should further improve the theoretical results. However, proper generation of intermolecular internal coordinates is still under investigation, not to mention the problem of managing the higher number of floppy degrees of freedom to handle.

4.2 Imidazole

The second test case is imidazole, with the Z-matrix defined in table 2. Imidazole derivatives are interesting as model systems for the more complex histidine molecule, so their spectroscopic properties can provide some insights on the latter's. Furthermore, due to the amphiphilic behaviour of the imidazole ring, it is usually significantly sensitive to the environment, and therefore it can be used as a probe in more complex systems, like proteins. Among the possible spectroscopic techniques, resonance Raman has been widely used both experimentally and theoretically,[96–98] since by tuning the incident wavelength to an electronic transition of imidazole, it is possible to enhance only the bands of the Raman spectrum localized on the imidazole ring, therefore eliminating the signals due to the environment. Like for 5,6-dimethyluracil, the theoretical approaches used so far to reproduce the RR spectrum of imidazole have been based on the VG model,[97,98] thus neglecting mode-mixing effects. The goal of this study is to compare the performance of the VG and AH models in the

reproduction of the overall band-shape, and to analyze the effects of the coordinate system on the theoretical results.

The incident wavelength has been set to the computed vertical energy of the first bright excited state of imidazole, corresponding to a $\pi \rightarrow \pi^\star$ transition, since the most recent experimental spectrum[98] has been recorded in resonance conditions with this excited state. The theoretical spectra calculated both in vacuum and in water using different coordinate systems are reported in figure 4. As before, PCM has been used to simulate solvent effects. It is noteworthy that the minimum of the excited state PES in vacuum corresponds to a planar geometry, and the difference with respect to the geometry of the ground state is nearly negligible. Since every non-redundant coordinate system is equivalent for infinitesimal distorsions from the reference geometry, the spectra computed with different coordinate set are nearly superimposable, as shown in the left panel of figure 4. This equivalence of the coordinate systems does not hold when solvation effects are included, since, in the minimum of the excited-state PES, the five-terms ring is distorted, as shown in figure 5. In this case, the theoretical spectrum simulated using cartesian coordinates presents very intense bands in the region between 600 cm^{-1} and 1000 cm^{-1}, corresponding to ring-deformation normal modes, which are not present in the experimental spectrum. Here again, Z-matrix coordinates are expected to perform poorly since a ring deformation is involved.[70] On the other hand, when delocalized internal coordinates are used, the intensity of the bands in the low-energy region of the spectrum decreases significantly. In order to highlight the differences between cartesian coordinates, DICs and ZICs, a graphical representation of the Duschinsky matrix $\mathbf{J}$ for the three coordinate systems is given in figure 6. It is noteworthy that the Duschinsky matrix is significantly less diagonal when ZICs are used, especially for the low-energy normal modes. This effect is a consequence of the poor description of those modes using standard Z-matrices, since the inaccurate reproduction of large-amplitude distortions introduces off-diagonal terms in $\mathbf{J}$, as already pointed out in other cases.[39,99] Similarly, in the cartesian representation non-negligible coupling terms are present between the low-

frequency normal modes and the high-energy ones. In conclusion, figure 7 shows a graphical representation of the shift vector **K** for the three different coordinate systems. In this case, the main consequence of the poor performance of cartesian and Z-matrix coordinates lies in the presence of an higher number of large components of **K**, since many modes must be shifted in order to describe only few large-amplitude deformations.

In order to check the reliability of different internal coordinate systems, the results obtained with ZICs and DICs are compared with experimental data, taken from ref.,[98] in figure 8. Even if the experimental spectrum has been recorded in the region between 1000 and 2000 cm^{-1}, and therefore the intense bands described above are outside this region, remarkable differences are observed with the two coordinate sets. In fact, when Z-matrix internal coordinates are used, the agreement between the theoretical and the experimental results is poor, and some bands are missing (as, for example, the two bands around 1500 cm^{-1}). On the other hand, when DICs are used, even if slight discrepancies are still present between the theoretical and experimental spectrum, it is possible to assign most of the intense bands of the experimental spectrum.

4.3 Tris(bipyridine)ruthenium(II) chloride

As a final test the reliability of our theoretical framework, let us consider the RR spectrum of a large-size metal complex. Indeed, since RR spectra of metal complexes are usually simpler than the non-resonant ones, due to the possibility of enhancing selectively vibrations of interest, the former technique is often preferred to study those kinds of systems. Additionally, the intensity of the peaks of a RR spectrum can be used to estimate geometry changes, as well as reorganization energies, upon electronic excitation.[100,101] Among the metal complexes which have been studied using RR spectroscopy, we will focus here on Tris(bipyridine)ruthenium(II) chloride (a graphical representation of its molecular structure is given in figure 9), which is usually considered as a model system for larger polypyridine ruthenium derivatives.[102,103] In fact, thanks to its relatively small dimension, simulations

using more refined vibronic models, involving the computation of the optimized geometry and the harmonic frequencies of the excited state, are still feasible.

The S_5 excited state, which corresponds to a metal-to-ligand charge-transfer transition, has been considered here as the intermediate state, since most of the experimental data are available in resonance with this electronic state.[103,104] The B3PW91 exchange-correlation functional, together with the LANL2DZ basis set, with pseudopotentials on core electrons of Ru and diffuse functions on C, N and Ru, has been employed. This computational protocol has been successfully applied to the study of the electronic properties a wide range of d^6 metal complexes,[105,106] and has been recently extended by some of us to the study of the vibronic properties of ruthenium compounds,[107] with particular focus on RR spectroscopy.[83] Our works have shown that, with a refined model like AH, together with a proper inclusion of solvent and anharmonicity effects, a quantitative agreement with experimental results can be reached.

Delocalized internal coordinates are well-suited for the study of metal complexes, since it is far from straightforward to build a complete, non-redundant Z-matrix for such complex molecular topologies, which involve several cyclic moieties. The difficulty is further enhanced if the Z-matrix must fulfill several symmetry constraints, and therefore ghost atoms must be used. On the other hand, the generation of DICs is rather simple, since only the topology of the complex needs to be defined.

Figure 10 shows the theoretical RR spectra of tris(bipyridine)ruthenium(II) calculated using both cartesian and delocalized internal coordinates at the AS (left panel) and AH levels. For both vibronic models, the spectra calculated using the different coordinate sets are nearly superimposable. The equivalence of the two coordinate systems is mainly due to the fact that no significant differences are present between the equilibrium geometries of the two electronic states. As a consequence, the description of the geometry deformation using the two different coordinate systems is equivalent, since they are indistinguishable for infinitesimal distorsions from the equilibrium position, as already pointed out. Therefore,

those results suggest that delocalized internal coordinates can be used as a standard in the simulation of vibronic spectra. In fact, as shown above, when large-amplitude deformations occur upon the electronic excitation, the results are significantly improved with respect to cartesian models, either adiabatic or vertical. On the other hand, when the equilibrium geometries of the two electronic states involved in the transition are similar, the results obtained using DICs are at least equivalent to those obtained in cartesian coordinates. Finally, DICs are rather easy to build also for large-size systems, whereas the definition of other internal coordinate systems is cumbersome for high coordination numbers, or when the molecular topology is complex.

5 Conclusions

In this work, a general time-dependent approach for the computation of RR spectra of flexible molecules, based on the use of internal coordinates, has been presented. This model relies on the harmonic approximation for the potential energy surfaces of both ground and excited states, and is based on the generalization of the definition of the Duschinsky transformation to a curvilinear, non-orthogonal set of coordinates. As illustrated with some medium-size organic and inorganic molecules used as test-cases, internal coordinates can improve remarkably the agreement between calculated and experimental spectra.

In order to use internal coordinates for the study of the spectroscopic properties of large-size molecules, an automatic algorithm to select a non-redundant set of internal coordinates must be devised. In this work, the performance of two automatic selection routes (Z-matrix and delocalized internal coordinates) have been tested and compared. Our results suggest that delocalized internal coordinates outperform the Z-matrix ones, especially for molecules with non-trivial topologies undergoing complex deformations upon the electronic excitation (like, for example, ring deformations). This result is coherent with what has been already shown also in the analysis of geometry optimization techniques in internal coordinates, where

the efficiency of Z-matrix coordinates is significantly lower than that of the delocalized ones for molecules with a complex topology.[70,71]

From another point of view, vertical models in cartesian coordinates are usually employed when the results obtained with adiabatic models in cartesian coordinates are inaccurate.[41,61] However, their use is often limited by the presence of one or more imaginary frequencies of the excited state PES at the vertical geometry, whose treatment faces a number of formal and technical problems, especially for medium- and large-size systems. In those cases, adiabatic models in internal coordinates could provide more reliable results, since both PESs are expanded around their own minimum, so that no imaginary frequencies are present in both electronic states.

Let us remark that the theoretical framework presented above requires further improvements. In fact, potential energy surfaces are usually highly anharmonic along large-amplitude normal modes, whereas our model heavily relies on the harmonic approximation. However, when internal coordinates are used, anharmonic couplings between different normal modes are significantly smaller with respect to the cartesian case. As a consequence, the inaccurate description of large-amplitude vibrations at the harmonic level does not affect the description of the other modes. Anyway, when large-amplitude modes have a strong impact on the experimental results, for example, if they are involved in a strong vibronic progression in one-photon spectra, or if intense bands are present in the low-energy region of a RR spectrum, any fully harmonic model becomes unreliable. In order to improve the accuracy of the theoretical results, hybrid schemes, where low-frequencies vibrations are treated at the anharmonic level, whereas the harmonic approximation is still used for the other ones, must be developed.

In conclusion, this work paves the route toward a systematic use of delocalized internal coordinates for the simulation of vibronic spectra of large-size systems. In fact, the internal coordinate framework presented above can be easily generalized to the simulation of different one-photon spectroscopies, both at the time-dependent and time-independent level, thanks

to a general framework introduced by some of us.[33–35]

Acknowledgment

This work was supported by the European Union (grant ERC-2012-AdG-320951-DREAMS) and Italian MIUR (FIRB 2012: Progettazione di materiali nano-eterogenei per la conversione di energia solare, protocollo: RBFR122HFZ). The high performance computer facilities of the DREAMS center (`http://dreamshpc.sns.it`) are acknowledged for providing computer resources.

References

(1) Asher, S. A. UV Resonance Raman Spectroscopy for Analytical, Physical, and Biophysical Chemistry. *Anal. Chem.* **1993**, *65*, 201A–210A.

(2) Benevides, J. M.; Overman, S. A.; Thomas, G. J. Raman, polarized Raman and ultraviolet resonance Raman spectroscopy of nucleic acids and their complexes. *J. Raman Spectrosc.* **2005**, *36*, 279–299.

(3) Efremov, E. V.; Ariese, F.; Gooijer, C. Achievements in resonance Raman spectroscopy: Review of a technique with a distinct analytical chemistry potential. *Anal. Chim. Acta* **2008**, *606*, 119 – 134.

(4) Kudelski, A. Analytical applications of Raman spectroscopy. *Talanta* **2008**, *76*, 1 – 8.

(5) Nafie, L. A. Recent advances in linear and nonlinear Raman spectroscopy. Part VIII. *J. Raman Spectrosc.* **2014**, *45*, 1326–1346.

(6) Zhang, S.-L. *Raman Spectroscopy and its Application in Nanostructures*; John Wiley & Sons, Ltd, 2012; pp 1–485.

(7) Vandenabeele, P.; Edwards, H. G. M.; Moens, L. A Decade of Raman Spectroscopy in Art and Archaeology. *Chem. Rev.* **2007**, *107*, 675–686.

(8) Mayhew, H. E.; Frano, K. A.; Svoboda, S. A.; Wustholz, K. L. Using Raman Spectroscopy and Surface-Enhanced Raman Scattering To Identify Colorants in Art: An Experiment for an Upper-Division Chemistry Laboratory. *J. Chem. Educ.* **2015**, *92*, 148–152.

(9) Long, D. A.; Long, D. *Raman spectroscopy*; McGraw-Hill New York, 1977; Vol. 206.

(10) Vandenabeele, P. *Practical Raman Spectroscopy - An Introduction*; John Wiley & Sons, Ltd, 2013; pp 1–38.

(11) Premvardhan, L.; Robert, B.; Beer, A.; Bächel, C. Pigment organization in fucoxanthin chlorophyll a/c2 proteins (FCP) based on resonance Raman spectroscopy and sequence analysis. *Biochim. Biophys. Acta* **2010**, *1797*, 1647 – 1656.

(12) Neugebauer, J. Chromophore-specific theoretical spectroscopy: From subsystem density functional theory to mode-specific vibrational spectroscopy. *Phys. Rep.* **2010**, *489*, 1 – 87.

(13) Biczysko, M.; Bloino, J.; Santoro, F.; Barone, V. In *Computational Strategies for Spectroscopy, from Small Molecules to Nano Systems*; Barone, V., Ed.; Wiley: Chichester, 2011; pp 361–443.

(14) Wilson, E. B. In *Molecular Vibrations: The Theory of Infrared and Raman Vibrational Spectra*; Dover,, Ed.; Dover Publications; New edition edition (March 1, 1980), 1980.

(15) Barone, V.; Baiardi, A.; Biczysko, M.; Bloino, J.; Cappelli, C.; Lipparini, F. Implementation and validation of a multi-purpose virtual spectrometer for large systems in complex environments. *Phys. Chem. Chem. Phys.* **2012**, *14*, 12404–12422.

(16) Scalmani, G.; Frisch, M. J.; Mennucci, B.; Tomasi, J.; Cammi, R.; Barone, V. Geometries and properties of excited states in the gas phase and in solution: Theory and application of a time-dependent density functional theory polarizable continuum model. *J. Chem. Phys.* **2006**, *124*, 94107–94115.

(17) Casida, M. E. Time-dependent density-functional theory for molecules and molecular solids. *J. Mol. Struct.* **2009**, *914*, 3–18.

(18) Barone, V.; Biczysko, M.; Bloino, J.; Carta, L.; Pedone, A. Environmental and dynamical effects on the optical properties of molecular systems by time-independent and time-dependent approaches: coumarin derivatives as test cases. *Comput. Theor. Chem.* **2014**, *1037*, 35–48.

(19) Lipparini, F.; Barone, V. Polarizable Force Fields and Polarizable Continuum Model: A Fluctuating Charges/PCM Approach. 1. Theory and Implementation. *J. Chem. Theory Comput.* **2011**, *7*, 3711–3724.

(20) Lipparini, F.; Cappelli, C.; Scalmani, G.; De Mitri, N.; Barone, V. Analytical First and Second Derivatives for a Fully Polarizable QM/Classical Hamiltonian. *J. Chem. Theory Comput.* **2012**, *8*, 4270–4278.

(21) Amovilli, C.; Barone, V.; Cammi, R.; Cancès, E.; Cossi, M.; Mennucci, B.; Pomelli, C. S.; Tomasi, J. Recent Advances in the Description of Solvent Effects with the Polarizable Continuum Model. *Adv. Quantum Chem.* **1998**, *32*, 227–261.

(22) Tomasi, J.; Mennucci, B.; Cammi, R. Quantum Mechanical Continuum Solvation Models. *Chem. Rev.* **2005**, *105*, 2999–3094.

(23) Aidas, K.; Mikkelsen, K. V.; Kongsted, J. Modelling spectroscopic properties of large molecular systems. The combined Density Functional Theory/Molecular Mechanics approach. *J. Comp. Methods in Sci. and Eng.* **2007**, *7*, 135–158.

(24) Sabin, J. R., Brandas, E., Eds. *Combining Quantum Mechanics and Molecular Mechanics. Some Recent Progresses in QM/MM Methods*; Advances in Quantum Chemistry; Academic Press, 2010; Vol. 59.

(25) Biczysko, M.; Bloino, J.; Brancato, G.; Cacelli, I.; Cappelli, C.; Ferretti, A.; Lami, A.; Monti, S.; Pedone, A.; Prampolini, G.; Puzzarini, C.; Santoro, F.; Trani, F.; Villani, G. Integrated Computational Approaches for Spectroscopic Studies of Molecular Systems in the Gas Phase and in Solution: Pyrimidine as a Test Case. *Theor. Chem. Acc.* **2012**, *131*, 1201/1–19.

(26) Berger, R.; Fischer, C.; Klessinger, M. Calculation of the Vibronic Fine Structure in Electronic Spectra at Higher Temperatures. 1. Benzene and Pyrazine. *J. Phys. Chem. A* **1998**, *102*, 7157–7167.

(27) Dierksen, M.; Grimme, S. Density functional calculations of the vibronic structure of electronic absorption spectra. *J. Chem. Phys.* **2004**, *120*, 3544–3554.

(28) Chang, J.-L. A new method to calculate Franck-Condon factors of multidimensional harmonic oscillators including the Duschinsky effect. *J. Chem. Phys.* **2008**, *128*, 174111.

(29) Tang, J.; Lee, M. T.; Lin, S. H. Effects of the Duschinsky mode-mixing mechanism on temperature dependence of electron transfer processes. *J. Chem. Phys.* **2003**, *119*, 7188–7196.

(30) Silverstein, D. W.; Jensen, L. Vibronic coupling simulations for linear and nonlinear optical processes: Theory. *J. Chem. Phys.* **2012**, *136*, 64111.

(31) Banerjee, S.; Saalfrank, P. Vibrationally resolved absorption, emission and resonance Raman spectra of diamondoids: a study based on time-dependent correlation functions. *Phys. Chem. Chem. Phys.* **2014**, *16*, 144–158.

(32) Santoro, F.; Improta, R.; Lami, A.; Bloino, J.; Barone, V. Effective method to compute Franck-Condon integrals for optical spectra of large molecules in solution. *J. Chem. Phys.* **2007**, *126*, 084509.

(33) Barone, V.; Bloino, J.; Biczysko, M.; Santoro, F. Fully Integrated Approach to Compute Vibrationally Resolved Optical Spectra: From Small Molecules to Macrosystems. *J. Chem. Theory Comput.* **2009**, *5*, 540–554.

(34) Bloino, J.; Biczysko, M.; Santoro, F.; Barone, V. General Approach to Compute Vibrationally Resolved One-Photon Electronic Spectra. *J. Chem. Theory Comput.* **2010**, *6*, 1256–1274.

(35) Baiardi, A.; Bloino, J.; Barone, V. General Time Dependent Approach to Vibronic

Spectroscopy Including Franck-Condon, Herzberg–Teller, and Duschinsky Effects. *J. Chem. Theory Comput.* **2013**, *9*, 4097–4115.

(36) Barone, V. Anharmonic vibrational properties by a fully automated second-order perturbative approach. *J. Chem. Phys.* **2005**, *122*, 14108.

(37) Bloino, J.; Biczysko, M.; Crescenzi, O.; Barone, V. Integrated computational approach to vibrationally resolved electronic spectra: Anisole as a test case. *J. Chem. Phys.* **2008**, *128*, 244105.

(38) Barone, V.; Biczysko, M.; Bloino, J. Fully anharmonic IR and Raman spectra of medium-size molecular systems: accuracy and interpretation. *Phys. Chem. Chem. Phys.* **2014**, *16*, 1759–1787.

(39) Borrelli, R.; Peluso, A. The electron photodetachment spectrum of c-C_4F_8: A test case for the computation of Franck-Condon factors of highly flexible molecules. *J. Chem. Phys.* **2008**, *128*, 44303.

(40) Peluso, A.; Borrelli, R.; Capobianco, A. Photoelectron Spectrum of Ammonia, a Test Case for the Calculation of Franck-Condon Factors in Molecules Undergoing Large Geometrical Displacements upon Photoionization. *J. Phys. Chem. A* **2009**, *113*, 14831–14837.

(41) Cerezo, J.; Zuniga, J.; Requena, A.; Avila Ferrer, F. J.; Santoro, F. Harmonic Models in Cartesian and Internal Coordinates to Simulate the Absorption Spectra of Carotenoids at Finite Temperatures. *J. Chem. Theory Comput.* **2013**, *9*, 4947–4958.

(42) Pulay, P.; Fogarasi, G. Geometry optimization in redundant internal coordinates. *J. Chem. Phys.* **1992**, *96*, 2856–2860.

(43) Baker, J.; Kessi, A.; Delley, B. The generation and use of delocalized internal coordinates in geometry optimization. *J. Chem. Phys.* **1996**, *105*, 192–212.

(44) Baker, J.; Kinghorn, D.; Pulay, P. Geometry optimization in delocalized internal coordinates: An efficient quadratically scaling algorithm for large molecules. *J. Chem. Phys.* **1999**, *110*, 4986–4991.

(45) Heller, E. J. The semiclassical way to molecular spectroscopy. *Acc. Chem. Res.* **1981**, *14*, 368–375.

(46) Heller, E. J. Time-dependent approach to semiclassical dynamics. *J. Chem. Phys.* **1975**, *62*, 1544–1555.

(47) Heller, E. J. Time dependent variational approach to semiclassical dynamics. *J. Chem. Phys.* **1976**, *64*, 63–73.

(48) Heller, E. J.; Sundberg, R.; Tannor, D. Simple aspects of Raman scattering. *J. Phys. Chem.* **1982**, *86*, 1822–1833.

(49) Tannor, D. J.; Heller, E. J. Polyatomic Raman scattering for general harmonic potentials. *J. Chem. Phys.* **1982**, *77*, 202–218.

(50) Neese, F.; Petrenko, T.; Ganyushin, D.; Olbrich, G. Advanced aspects of ab initio theoretical optical spectroscopy of transition metal complexes: Multiplets, spin-orbit coupling and resonance Raman intensities. *Coord. Chem. Rev.* **2007**, *251*, 288 – 327.

(51) Silverstein, D. W.; Jensen, L. Vibronic coupling simulations for linear and nonlinear optical processes: Simulation results. *J. Chem. Phys.* **2012**, *136*, 64110.

(52) Ma, H.; Liu, J.; Liang, W. Time-Dependent Approach to Resonance Raman Spectra Including Duschinsky Rotation and Herzberg–Teller Effects: Formalism and Its Realistic Applications. *J. Chem. Theory Comput.* **2012**, *8*, 4474–4482.

(53) Banerjee, S.; Kröner, D.; Saalfrank, P. Resonance Raman and vibronic absorption spectra with Duschinsky rotation from a time-dependent perspective: Application to β-carotene. *J. Chem. Phys.* **2012**, *137*, 22A534.

(54) Baiardi, A.; Bloino, J.; Barone, V. A general time-dependent route to Resonance-Raman spectroscopy including Franck-Condon, Herzberg–Teller and Duschinsky effects. *J. Chem. Phys.* **2014**, *141*, 114108.

(55) Beenken, W. J. D.; Lischka, H. Spectral broadening and diffusion by torsional motion in biphenyl. *J. Chem. Phys.* **2005**, *123*, 144311.

(56) Reimers, J. R. A practical method for the use of curvilinear coordinates in calculations of normal-mode-projected displacements and Duschinsky rotation matrices for large molecules. *J. Chem. Phys.* **2001**, *115*, 9103–9109.

(57) Natanson, G. A.; Garrett, B. C.; Truong, T. N.; Joseph, T.; Truhlar, D. G. The definition of reaction coordinates for reaction-path dynamics. *J. Chem. Phys.* **1991**, *94*, 7875–7892.

(58) Jackels, C. F.; Gu, Z.; Truhlar, D. G. Reaction path potential and vibrational frequencies in terms of curvilinear internal coordinates. *J. Chem. Phys.* **1995**, *102*, 3188–3201.

(59) Miyazawa, T. Symmetrization of Secular Determinant for Normal Vibration Calculation. *J. Chem. Phys.* **1958**, *29*, 246–246.

(60) Brandhorst, K.; Grunenberg, J. Efficient computation of compliance matrices in redundant internal coordinates from Cartesian Hessians for nonstationary points. *J. Chem. Phys.* **2010**, *132*, 184101.

(61) Götze, J. P.; Karasulu, B.; Thiel, W. Computing UV/vis spectra from the adiabatic and vertical Franck-Condon schemes with the use of Cartesian and internal coordinates. *J. Chem. Phys.* **2013**, *139*, 234108.

(62) Karasulu, B.; Götze, J. P.; Thiel, W. Assessment of Franck-Condon Methods for Computing Vibrationally Broadened UV-vis Absorption Spectra of Flavin Derivatives:

Riboflavin, Roseoflavin, and 5-Thioflavin. *J. Chem. Theory Comput.* **2014**, *10*, 5549–5566.

(63) von Arnim, M.; Ahlrichs, R. Geometry optimization in generalized natural internal coordinates. *J. Chem. Phys.* **1999**, *111*, 9183–9190.

(64) Lindh, R.; Bernhardsson, A.; Schätz, M. Force-constant weighted redundant coordinates in molecular geometry optimizations. *Chem. Phys. Lett.* **1999**, *303*, 567 – 575.

(65) Pulay, P.; Fogarasi, G.; Pongor, G.; Boggs, J. E.; Vargha, A. Combination of theoretical ab initio and experimental information to obtain reliable harmonic force constants. Scaled quantum mechanical (QM) force fields for glyoxal, acrolein, butadiene, formaldehyde, and ethylene. *J. Am. Chem. Soc.* **1983**, *105*, 7037–7047.

(66) Pulay, P.; Fogarasi, G.; Zhou, X.; Taylor, P. W. Ab initio prediction of vibrational spectra: A database approach. *Vib. Spectrosc.* **1990**, *1*, 159 – 165.

(67) Rauhut, G.; Pulay, P. Transferable Scaling Factors for Density Functional Derived Vibrational Force Fields. *J. Phys. Chem.* **1995**, *99*, 3093–3100.

(68) Baker, J.; Jarzecki, A. A.; Pulay, P. Direct Scaling of Primitive Valence Force Constants: An Alternative Approach to Scaled Quantum Mechanical Force Fields. *J. Phys. Chem. A* **1998**, *102*, 1412–1424.

(69) Jensen, F.; Palmer, D. S. Harmonic Vibrational Analysis in Delocalized Internal Coordinates. *J. Chem. Theory Comput.* **2011**, *7*, 223–230.

(70) Baker, J.; Hehre, W. J. Geometry optimization in cartesian coordinates: The end of the Z-matrix? *J. Comput. Chem.* **1991**, *12*, 606–610.

(71) Baker, J.; Chan, F. The location of transition states: A comparison of Cartesian, Z-matrix, and natural internal coordinates. *J. Comput. Chem.* **1996**, *17*, 888–904.

(72) Swart, M.; Matthias Bickelhaupt, F. Optimization of strong and weak coordinates. *Int. J. Quantum Chem.* **2006**, *106*, 2536–2544.

(73) Frisch, M. J.; Trucks, G. W.; Schlegel, H. B.; Scuseria, G. E.; Robb, M. A.; Cheeseman, J. R.; Scalmani, G.; Barone, V.; Mennucci, B.; Petersson, G. A.; Nakatsuji, H.; Caricato, M.; Li, X.; Hratchian, H. P.; Bloino, J.; Janesko, B. G.; Izmaylov, A. F.; Lipparini, F.; Zheng, G.; Sonnenberg, J. L.; Liang, W.; Hada, M.; Ehara, M.; Toyota, K.; Fukuda, R.; Hasegawa, J.; Ishida, M.; Nakajima, T.; Honda, Y.; Kitao, O.; Nakai, H.; Vreven, T.; Throssell, K.; Montgomery Jr., J. A.; Peralta, J. E.; Ogliaro, F.; Bearpark, M.; Heyd, J. J.; Brothers, E.; Kudin, K. N.; Staroverov, V. N.; Keith, T.; Kobayashi, R.; Normand, J.; Raghavachari, K.; Rendell, A.; Burant, J. C.; Iyengar, S. S.; Tomasi, J.; Cossi, M.; Rega, N.; Millam, J. M.; Klene, M.; Knox, J. E.; Cross, J. B.; Bakken, V.; Adamo, C.; Jaramillo, J.; Gomperts, R.; Stratmann, R. E.; Yazyev, O.; Austin, A. J.; Cammi, R.; Pomelli, C.; Ochterski, J. W.; Martin, R. L.; Morokuma, K.; Zakrzewski, V. G.; Voth, G. A.; Salvador, P.; Dannenberg, J. J.; Dapprich, S.; Parandekar, P. V.; Mayhall, N. J.; Daniels, A. D.; Farkas, O.; Foresman, J. B.; Ortiz, J. V.; Cioslowski, J.; Fox, D. J. Gaussian Development Version, Revision I.03. 2015; Gaussian, Inc., Wallingford CT.

(74) Becke, A. D. Density-functional Thermochemistry. III. The Role of Exact Exchange. *J. Chem. Phys.* **1993**, *98*, 5648–5652.

(75) Double and triple-ζ basis sets of SNS family, are available for download. http://compchem.sns.it/downloads. `http://compchem.sns.it/downloads`.

(76) Barone, V.; Cimino, P. Accurate and feasible computations of structural and magnetic properties of large free radicals: The PBE0/N07D model. *Chem. Phys. Lett.* **2008**, *454*, 139–143.

(77) Barone, V.; Cimino, P.; Stendardo, E. Development and Validation of the

B3LYP/N07D Computational Model for Structural Parameter and Magnetic Tensors of Large Free Radicals. *J. Chem. Theory Comput.* **2008**, *4*, 751–764.

(78) Egidi, F.; Bloino, J.; Cappelli, C.; Barone, V. A Robust and Effective Time-Independent Route to the Calculation of Resonance Raman Spectra of Large Molecules in Condensed Phases with the Inclusion of Duschinsky, Herzberg-Teller, Anharmonic, and Environmental Effects. *J. Chem. Theory Comput.* **2014**, *10*, 346–363.

(79) Kendall, R. A.; Dunning, T. H.; Harrison, R. J. Electron affinities of the first-row atoms revisited. Systematic basis sets and wave functions. *J. Chem. Phys.* **1992**, *96*, 6796–6806.

(80) Mennucci, B. Polarizable continuum model. *Wiley Interdiscip. Rev.: Comput. Mol. Sci.* **2012**, *2*, 386–404.

(81) Cances, E.; Mennucci, B.; Tomasi, J. A new integral equation formalism for the polarizable continuum model: Theoretical background and applications to isotropic and anisotropic dielectrics. *J. Chem. Phys.* **1997**, *107*, 3032–3041.

(82) Santoro, F.; Cappelli, C.; Barone, V. Effective Time-Independent Calculations of Vibrational Resonance Raman Spectra of Isolated and Solvated Molecules Including Duschinsky and Herzberg-Teller Effects. *J. Chem. Theory Comput.* **2011**, *7*, 1824–1839.

(83) Baiardi, A.; Latouche, C.; Bloino, J.; Barone, V. Accurate yet feasible computations of resonance Raman spectra for metal complexes in solution: $[Ru(bpy)^3]^{2+}$ as a case study. *Dalton Trans.* **2014**, *43*, 17610–17614.

(84) Bakken, V.; Helgaker, T. The efficient optimization of molecular geometries using redundant internal coordinates. *J. Chem. Phys.* **2002**, *117*, 9160–9174.

(85) Avila Ferrer, F. J.; Barone, V.; Cappelli, C.; Santoro, F. Duschinsky, Herzberg-Teller, and Multiple Electronic Resonance Interferential Effects in Resonance Raman Spectra and Excitation Profiles. The Case of Pyrene. *J. Chem. Theory Comput.* **2013**, *9*, 3597–3611.

(86) Licari, D.; Baiardi, A.; Biczysko, M.; Egidi, F.; Latouche, C.; Barone, V. Implementation of a graphical user interface for the virtual multifrequency spectrometer: The VMS-Draw tool. *J. Comput. Chem.* **2015**, *36*, 321–334.

(87) Ismail, N.; Blancafort, L.; Olivucci, M.; Kohler, B.; Robb, M. A. Ultrafast Decay of Electronically Excited Singlet Cytosine via a π,$\pi^\star$ to n,$\pi^\star$ State Switch. *J. Am. Chem. Soc.* **2002**, *124*, 6818–6819.

(88) Crespo-Hernandez, C. E.; Cohen, B.; Hare, P. M.; Kohler, B. Ultrafast Excited-State Dynamics in Nucleic Acids. *Chem. Rev.* **2004**, *104*, 1977–2020.

(89) Improta, R.; Barone, V. Absorption and Fluorescence Spectra of Uracil in the Gas Phase and in Aqueous Solution: A TD-DFT Quantum Mechanical Study. *J. Am. Chem. Soc.* **2004**, *126*, 14320–14321.

(90) Billinghurst, B. E.; Loppnow, G. R. Excited-State Structural Dynamics of Cytosine from Resonance Raman Spectroscopy. *J. Phys. Chem. A* **2006**, *110*, 2353–2359.

(91) Yarasi, S.; Ng, S.; Loppnow, G. R. Initial Excited-State Structural Dynamics of Uracil from Resonance Raman Spectroscopy Are Different from Those of Thymine (5-Methyluracil). *J. Phys. Chem. B* **2009**, *113*, 14336–14342.

(92) Sasidharanpillai, S.; Loppnow, G. R. Initial Excited-State Structural Dynamics of 5,6-Dimethyluracil from Resonance Raman Spectroscopy. *J. Phys. Chem. A* **2014**, *118*, 4680–4687.

(93) Peticolas, W. L.; Rush, T. Ab initio calculations of the ultraviolet resonance Raman spectra of uracil. *J. Comput. Chem.* **1995**, *16*, 1261–1270.

(94) Neugebauer, J.; Hess, B. A. Resonance Raman spectra of uracil based on Kramers-Kronig relations using time-dependent density functional calculations and multireference perturbation theory. *J. Chem. Phys.* **2004**, *120*, 11564–11577.

(95) Sun, S.; Brown, A. Simulation of the Resonance Raman Spectrum for Uracil. *J. Phys. Chem. A* **2014**, *118*, 9928.

(96) Jarzecki, A. A.; Spiro, T. G. Ab initio computation of the UV resonance Raman intensity pattern of aqueous imidazole. *J. Raman Spectrosc.* **2001**, *32*, 599–605.

(97) Jarzecki, A. A. Quantum-Mechanical Calculations of Resonance Raman Intensities: The Weighted-Gradient Approximation. *J. Phys. Chem. A* **2009**, *113*, 2926–2934.

(98) Balakrishnan, G.; Jarzecki, A. A.; Wu, Q.; Kozlowski, P. M.; Wang, D.; Spiro, T. G. Mode Recognition in UV Resonance Raman Spectra of Imidazole: Histidine Monitoring in Proteins. *J. Phys. Chem. B* **2012**, *116*, 9387–9395.

(99) Borrelli, R.; Peluso, A. The vibrational progressions of the N-V electronic transition of ethylene: A test case for the computation of Franck-Condon factors of highly flexible photoexcited molecules. *J. Chem. Phys.* **2006**, *125*, 194308.

(100) Myers, A. B. Resonance Raman Intensities and Charge-Transfer Reorganization Energies. *Chem. Rev.* **1996**, *96*, 911–926.

(101) Wachtler, M.; Guthmuller, J.; Gonzalez, L.; Dietzek, B. Analysis and characterization of coordination compounds by resonance Raman spectroscopy. *Coord. Chem. Rev.* **2012**, *256*, 1479 – 1508.

(102) Omberg, K. M.; Schoonover, J. R.; Treadway, J. A.; Leasure, R. M.; Dyer, R. B.;

Meyer, T. J. Mid-Infrared Spectrum of $[Ru(bpy)_3]^{2+*}$. *J. Am. Chem. Soc.* **1997**, *119*, 7013–7018.

(103) Adam Webb, M.; Knorr, F. J.; McHale, J. L. Resonance Raman spectrum of $[Ru(bipyridine)_3]^{2+}$ in water, acetonitrile and their deuterated derivatives: the possible role of solvent in excited-state charge localization. *J. Raman Spectrosc.* **2001**, *32*, 481–485.

(104) Basu, A.; Gafney, H. D.; Strekas, T. C. Resonance Raman spectra of ruthenium(II) complexes of bipyridine and substituted bipyridines: ground- and excited-state properties. *Inorg. Chem.* **1982**, *21*, 2231–2235.

(105) Tsai, C.-N.; Allard, M. M.; Lord, R. L.; Luo, D.-W.; Chen, Y.-J.; Schlegel, H. B.; Endicott, J. F. Characterization of Low Energy Charge Transfer Transitions in (terpyridine)(bipyridine)Ruthenium(II) Complexes and their Cyanide-Bridged Bi- and Tri-Metallic Analogues. *Inorg. Chem.* **2011**, *50*, 11965–11977.

(106) Bortoluzzi, M.; Paolucci, G.; Pitteri, B. Ground-state properties of ruthenium(II) and osmium(II) tin trihydride complexes: A DFT study. *Polyhedron* **2011**, *30*, 1524 – 1529.

(107) Latouche, C.; Baiardi, A.; Barone, V. Virtual Eyes Designed for Quantitative Spectroscopy of Inorganic Complexes: Vibronic Signatures in the Phosphorescence Spectra of Terpyridine Derivatives. *J. Phys. Chem. B* **2015**,

Figures

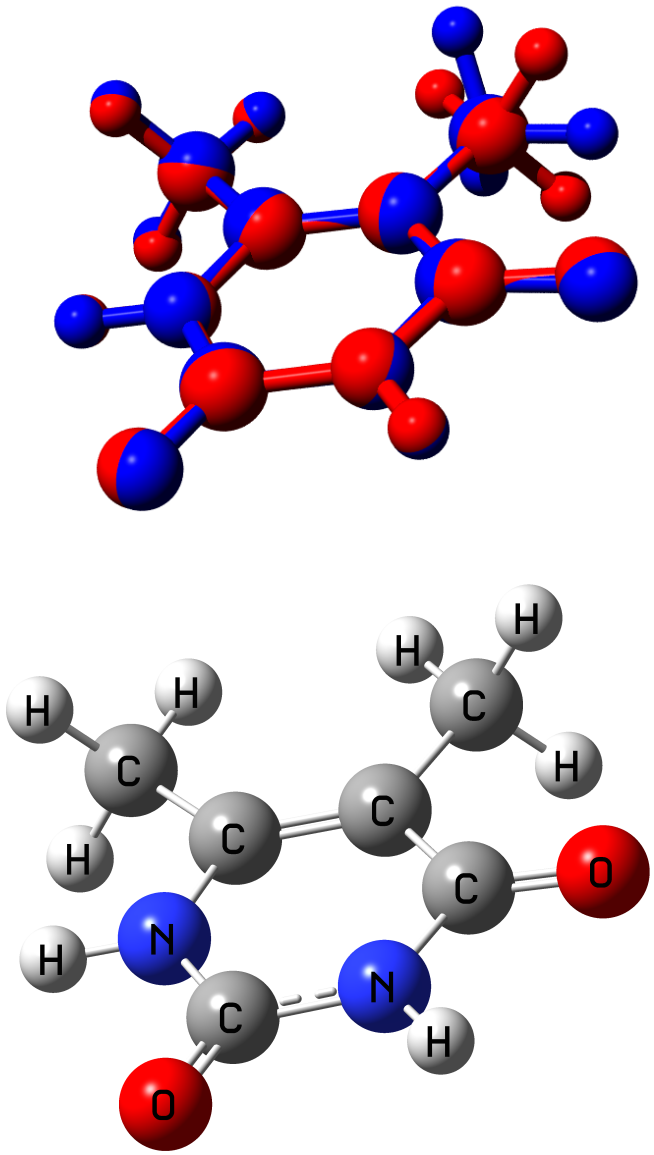

Figure 1: Superposition of the optimized geometries of the S_0 (in red) and S_2 (in blue) electronic states of 5,6-dimethyluracil. The S_0 structure is used as reference for the atom type definition (bottom structure).

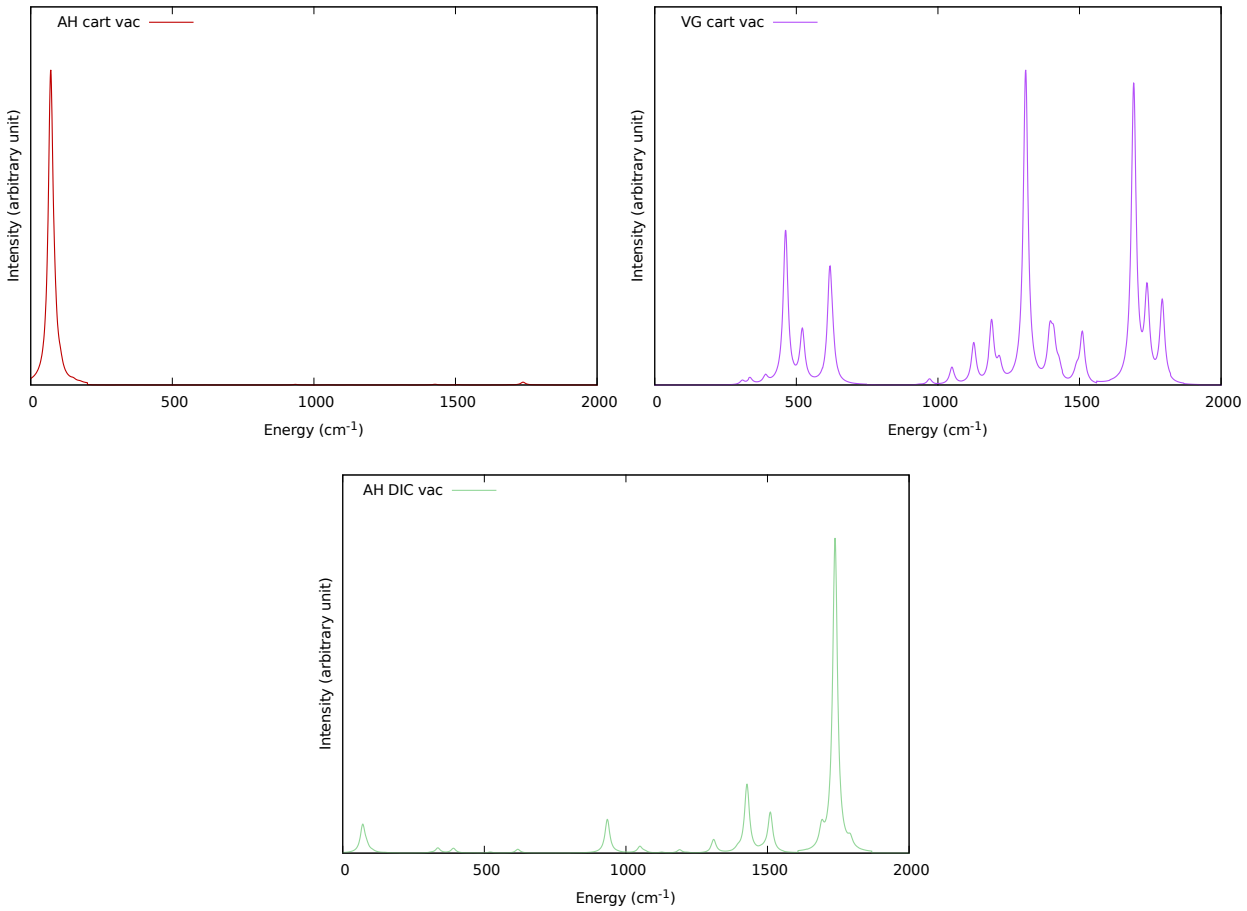

Figure 2: Comparison of the theoretical RR spectra of 5,6-dimethyluracil calculated by using different coordinates system and different models for the excited state PES: AH in cartesian coordinates (upper panel, left), VG in cartesian coordinates (upper panel, right), AH in delocalized internal coordinates (lower panel). The intensity of each spectrum has been rescaled with respect to the most intense band, and Lorentzian distribution functions with an half-width at half-maximum of 10 cm^{-1} have been applied to each peak to reproduce broadening effects.

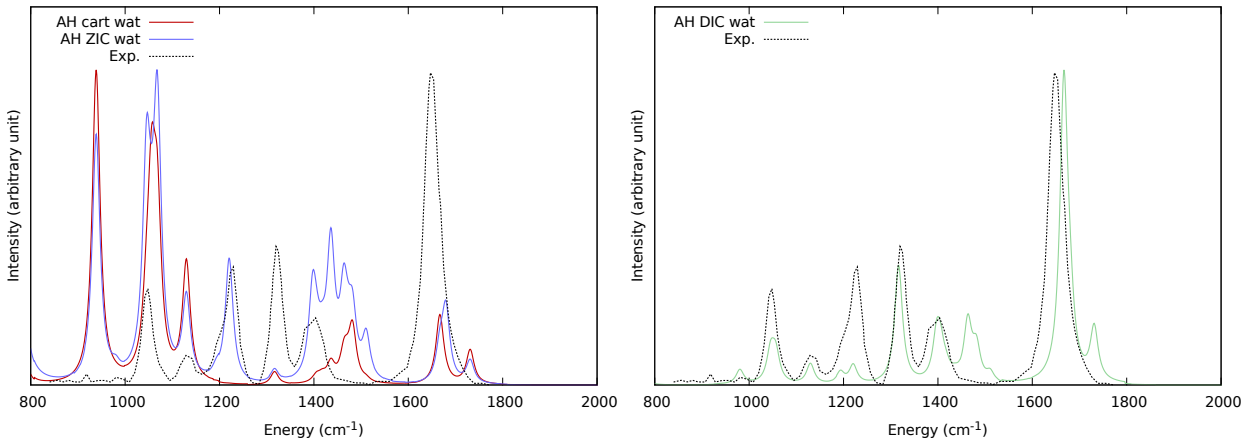

Figure 3: Comparison of the theoretical and experimental RR spectrum of 5,6-dimethyluracil (taken from ref.[92]). Vibronic calculations were performed at the AH level with cartesian and Z-matrix coordinates (left panel) and delocalized internal coordinates (right panel). Solvent effects have been included within PCM. The intensity of each spectrum has been rescaled with respect to the most intense band, and Lorentzian distribution functions with an half-width at half-maximum of 10 cm^{-1} have been applied to each peak to reproduce broadening effects.

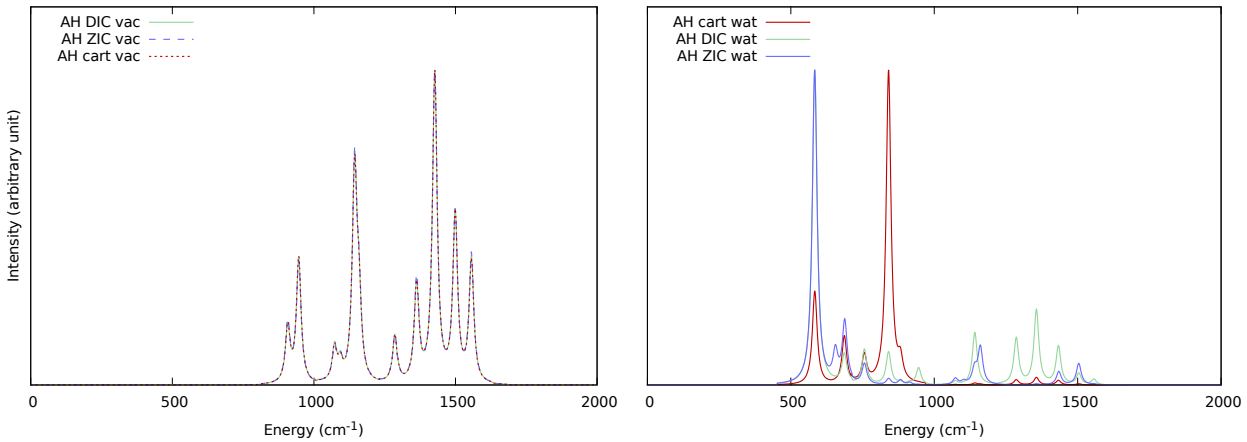

Figure 4: Comparison of the RR spectrum of imidazole calculated at the AH level using different coordinate systems: cartesian (red line), Z-matrix (green line) and delocalized internal coordinates (blue line) in vacuum (left panel) and in water (right panel). Solvent effects have been included with PCM. The intensity of each spectrum has been rescaled with respect to the most intense band, and Lorentzian distribution functions with an half-width at half-maximum of 10 cm^{-1} have been applied to each peak to reproduce broadening effects.

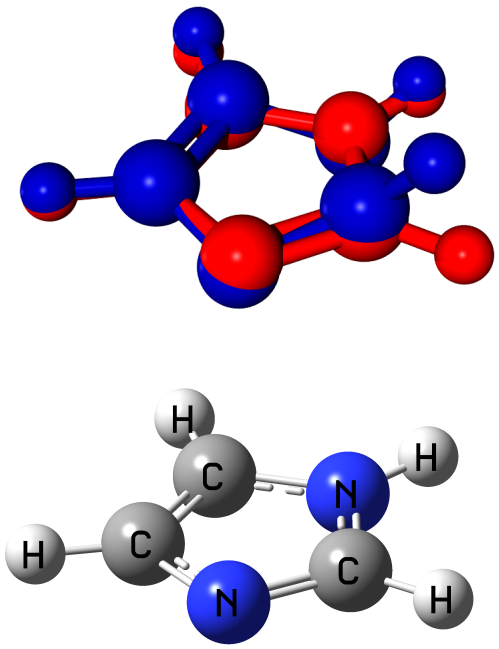

Figure 5: Superposition of the optimized geometries of the S_0 (in red) and S_1 (in blue) electronic states of imidazole. The S_0 structure is used as reference for the atom type definition (bottom structure).

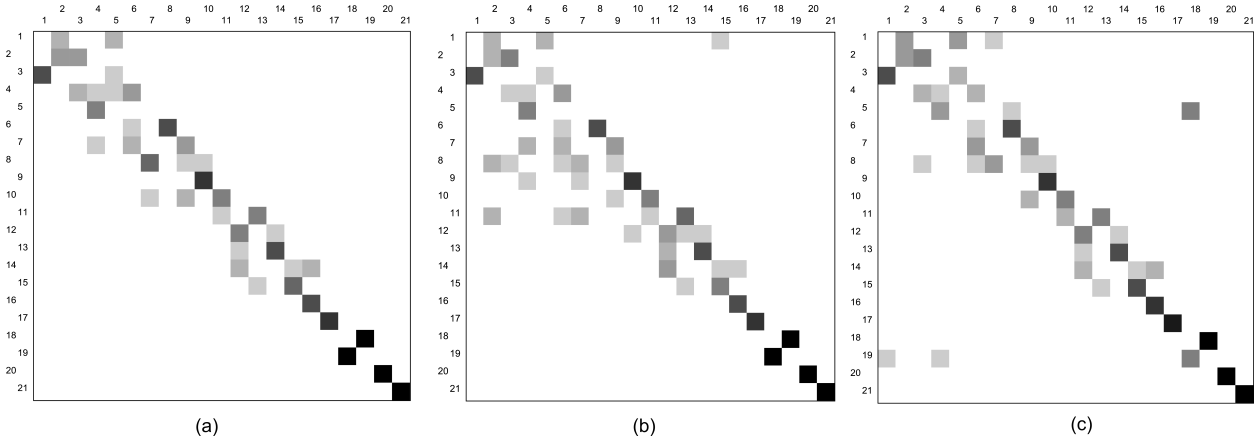

Figure 6: Graphical representation of the Duschinsky matrix for the $\pi \longrightarrow \pi^*$ transition of imidazole in water using delocalized (a), z-matrix (b) and cartesian (c) coordinates. The representation is obtained as follows: the elements J_{ij}^2 are calculated and a shade of gray is associated to each element (i,j) in the figure based on the equivalence (0, white; 1, black). The normal modes are sorted in increasing order of frequency.

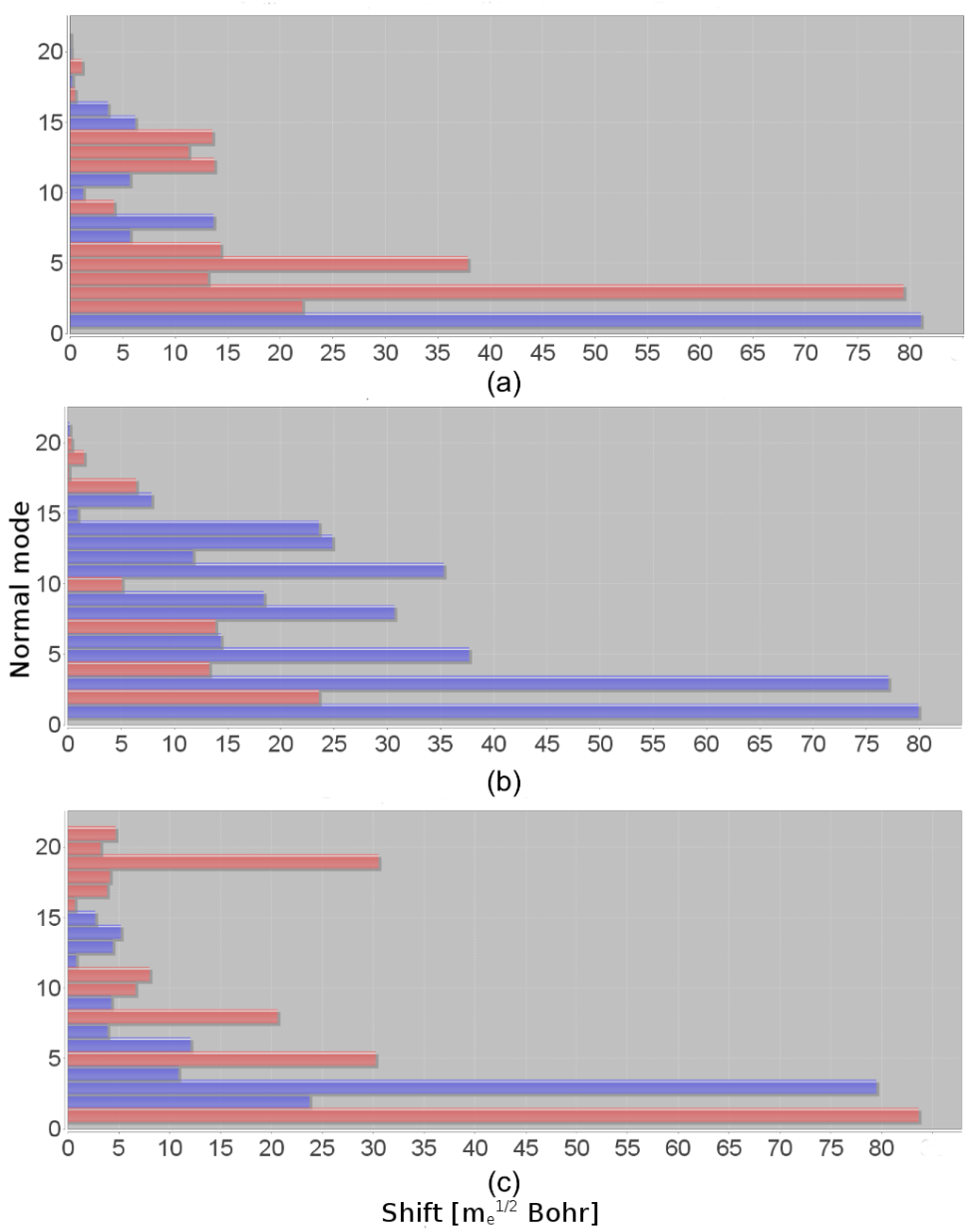

Figure 7: Graphical representation of the Shift vector for the $\pi \longrightarrow \pi^*$ transition of imidazole in water using delocalized (a), z-matrix (b) and cartesian (c) coordinates. On the y axis the indexes of the normal modes, sorted in increasing order of frequency, are reported, while on the x axis the absolute value of the associated component of the shift vector $\mathbf{K}$ (in Bohr $\times$ au$^{1/2}$) is reported. Red and blue bars are associated to positive and negative values of the shift vector, respectively.

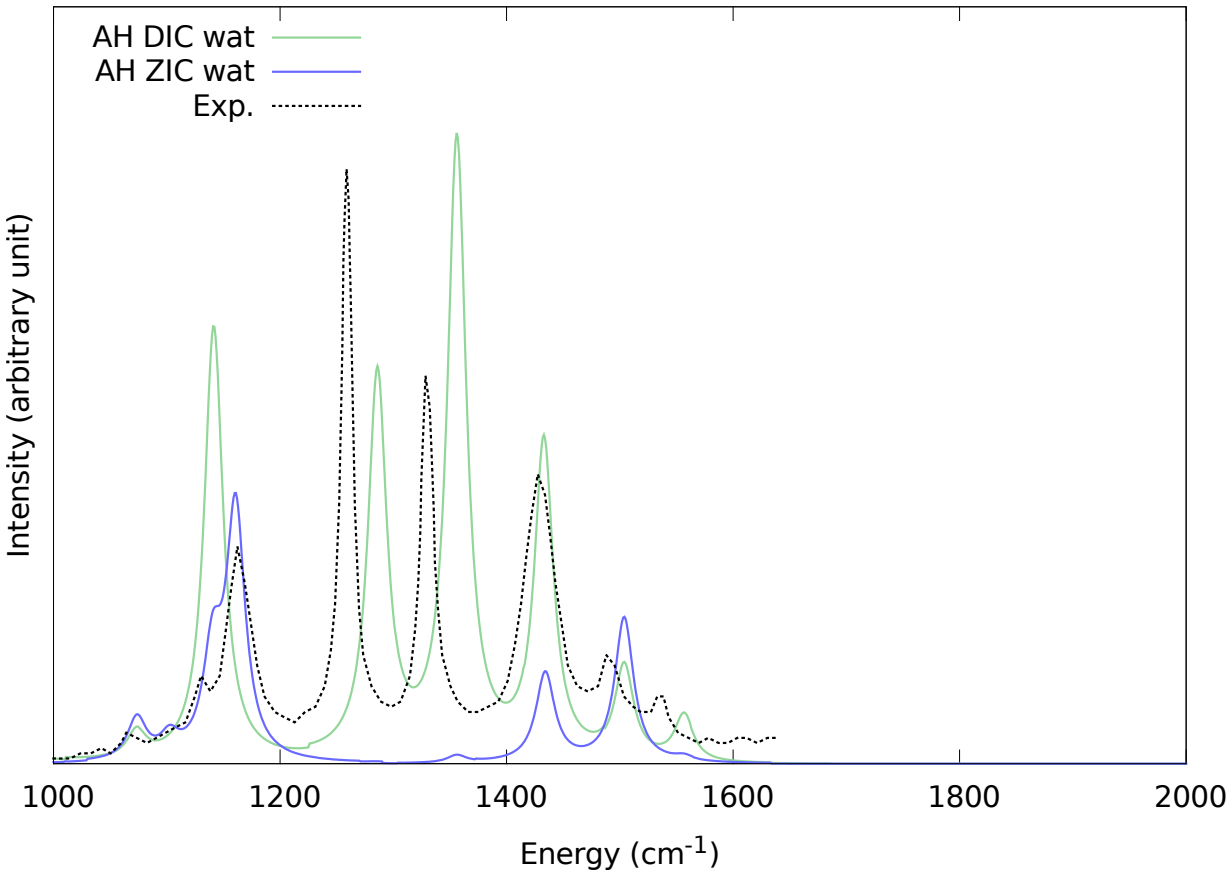

Figure 8: Comparison of the RR spectrum of imidazole calculated at the AH level in the region between 1000 and 2000 cm^{-1} using Z-matrix (green line) and delocalized internal coordinates in water. Solvent effects have been included by means of PCM. The intensity of each spectrum has been rescaled with respect to the most intense band, and Lorentzian distribution functions with an half-width at half-maximum of 10 cm^{-1} have been applied to each peak to reproduce broadening effects. The experimental spectrum is taken from ref.[98]

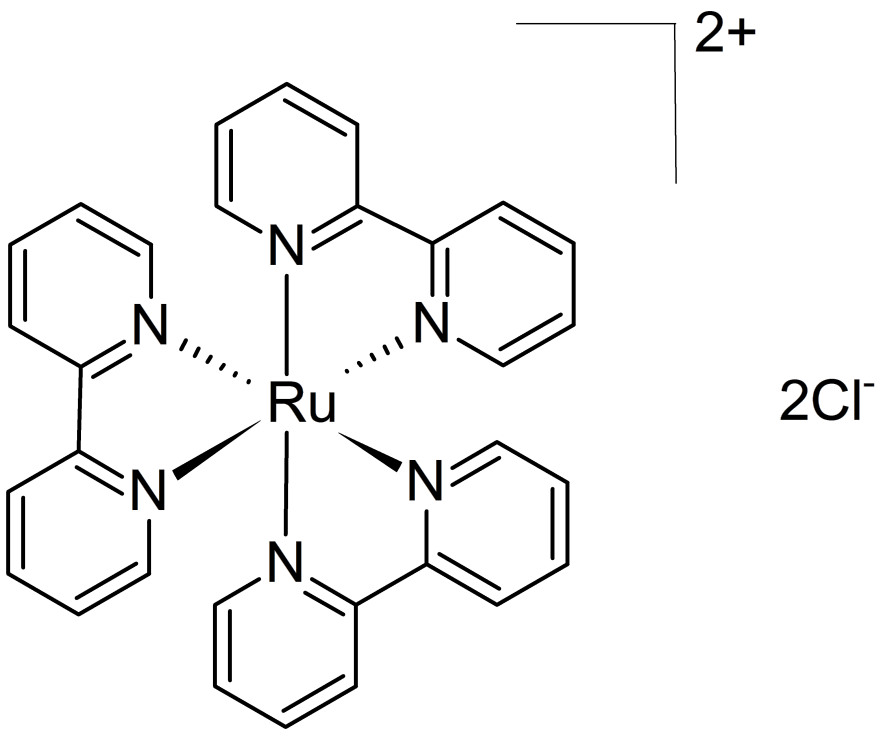

Figure 9: Graphical representation of the structure of Tris(bipyridine)ruthenium(II) chloride

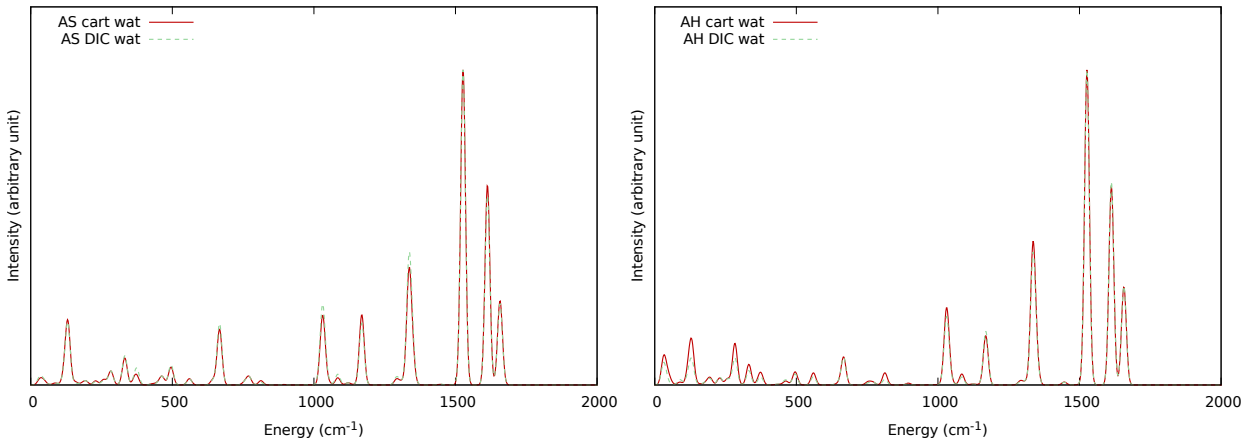

Figure 10: Comparison of the RR spectrum of Tris(bipyridine)ruthenium(II) chloride calculated at the AS (left panel) and AH levels using cartesian (dashed line) and delocalized internal coordinates (solid line). Solvent effects have been included by means of PCM. The intensity of each spectrum has been rescaled with respect to the most intense band, and Lorentzian distribution functions with an half-width at half-maximum of 10 cm^{-1} have been applied to each peak to reproduce broadening effects.

6 Tables

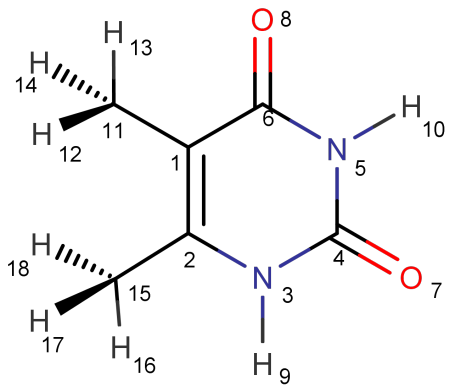

	Bond length	Valence angle	Dihedral angle
1	$r_{1,2}$		
2	$r_{2,3}$	$\alpha_{3,2,1}$	
3	$r_{3,4}$	$\alpha_{4,3,2}$	$\delta_{4,3,2,1}$
4	$r_{4,5}$	$\alpha_{5,4,3}$	$\delta_{5,4,3,2}$
5	$r_{5,6}$	$\alpha_{6,5,4}$	$\delta_{6,5,4,3}$
6	$r_{4,7}$	$\alpha_{7,4,3}$	$\delta_{7,4,3,2}$
7	$r_{6,8}$	$\alpha_{8,6,5}$	$\delta_{8,6,5,4}$
8	$r_{3,9}$	$\alpha_{9,3,2}$	$\delta_{9,3,2,1}$
9	$r_{5,10}$	$\alpha_{10,5,4}$	$\delta_{10,5,4,3}$
10	$r_{1,11}$	$\alpha_{11,1,2}$	$\delta_{11,1,2,3}$
11	$r_{11,12}$	$\alpha_{12,11,1}$	$\delta_{12,11,1,2}$
12	$r_{11,13}$	$\alpha_{13,11,1}$	$\delta_{13,11,1,2}$
13	$r_{11,14}$	$\alpha_{14,11,1}$	$\delta_{14,11,1,2}$
14	$r_{2,15}$	$\alpha_{15,2,1}$	$\delta_{15,2,1,6}$
15	$r_{15,16}$	$\alpha_{16,15,2}$	$\delta_{16,15,2,1}$
16	$r_{15,17}$	$\alpha_{17,15,2}$	$\delta_{17,15,2,1}$
17	$r_{15,18}$	$\alpha_{18,15,2}$	$\delta_{18,15,2,1}$

Table 1: Definition of the Z-matrix coordinates for 5,6-dimethyluracil

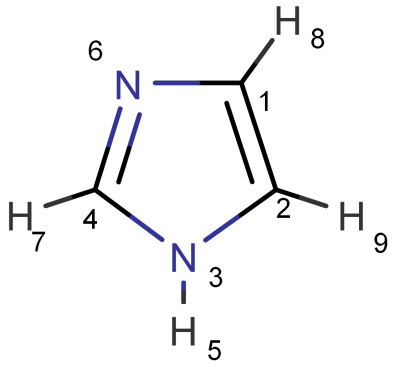

	Bond length	Valence angle	Dihedral angle
1	$r_{1,2}$		
2	$r_{2,3}$	$\alpha_{3,2,1}$	
3	$r_{3,4}$	$\alpha_{4,3,2}$	$\delta_{4,3,2,1}$
4	$r_{3,5}$	$\alpha_{5,3,2}$	$\delta_{5,3,2,1}$
5	$r_{4,6}$	$\alpha_{6,4,3}$	$\delta_{6,4,3,2}$
6	$r_{4,7}$	$\alpha_{7,4,3}$	$\delta_{7,4,3,2}$
7	$r_{8,1}$	$\alpha_{8,1,2}$	$\delta_{8,1,2,3}$
8	$r_{9,2}$	$\alpha_{9,2,1}$	$\delta_{9,2,1,3}$

Table 2: Definition of the Z-matrix coordinates for imidazole